INORGANIC CHEMISTRY
FRONTIERS

RESEARCH ARTICLE

View Article Online
View Journal | View Issue

Cite this: *Inorg. Chem. Front.*, 2025, **12**, 8470

Anion exchange in bismuth oxyhalides for electronic property control and isolation of $BiON_3$

Alexander E. Padilla II and Adam Jaffe *

Bismuth oxyhalides are a class of layered materials with rich potential for chemical and electronic tuning through anionic substitution, including the less-explored incorporation of pseudohalides such as azide (N_3^-). Here, we develop three synthetic strategies for the synthesis of $BiON_3$: post-synthetic exchange, solvothermal synthesis, and coprecipitation. We present the first structural model for $BiON_3$ that is supported by Rietveld refinement, revealing a highly disordered structure that features interdigitated azide molecules between the layers. We then probe the effects of heteroanion incorporation on the electronic structure of $BiON_3$, including through the synthesis of mixed azide/iodide systems. Further, we demonstrate intriguing thermally induced reactivity in $BiON_3$ that is suggestive of N atom transfer and subsequent gas evolution. This work considerably expands the available routes for synthetic control of this promising material platform.

Received 30th July 2025,
Accepted 14th September 2025

DOI: 10.1039/d5qi01602a

rsc.li/frontiers-inorganic

Introduction

Two-dimensional mixed-anion bismuth materials featuring $[Bi_2O_2]^{2+}$ layers in their underlying frameworks have been extensively studied over the past century for their relevance to photocatalysis, photovoltaics, and optoelectronics.[1–5] This functionality can be attributed in part to the fact that these cationic bismuth oxide slabs support a variety of anionic species, X, such as halides and chalcogenides, that allow for fine-tuning of the compounds' electronic band structures.[6] Specifically, anion substitution modifies orbital contributions to the valence band, tuning the valence band maximum position and subsequently the band gap of the material.[7–9] These $[Bi_2O_2]^{2+}$ materials' anisotropic 2D layered structures also support internal static electric fields that facilitate the separation of photoinduced charge carriers.[10,11] Further, the electronic behavior of $[Bi_2O_2]^{2+}$-based materials can be tuned through control of particle morphologies.[11–13]

Recent studies focusing on modifying bismuth oxyanion materials through heteroatomic substitution have done so through heteroatom doping (*i.e.*, small concentrations),[14] tuning of anion solid solution compositions[14] and non-stoichiometric ($Bi_xO_yX_z$) phases,[15,16] or even through complete exchange of anions to access new materials.[17–19] For example, the substitution of chloride ions with carbodiimide ions in BiOCl *via* a solid-state metathesis reaction was recently shown to significantly modify the band gap from 3.4 eV in the parent BiOCl material to 1.8 eV for the resulting product.[18] The structurally related Bi_2O_2S exhibits an even lower band gap of 1.12 eV.[18,20] Another recent study showcased iodide doping and solid solution formation in BiOX materials.[14] The authors observed sub-gap photoemission they attributed to self-trapped excitonic states whose energies could be tuned through compositional alloying. Thus, anion exchange represents a powerful design tool for the optical and electronic modification and control of $[Bi_2O_2]^{2+}$ materials and we direct the reader's attention to a number of extensive reviews that have covered this subject.[6,9,17–19]

Despite this widespread investigation of anion substitution in $[Bi_2O_2]^{2+}$ materials, few works have explored the incorporation of so-called pseudohalide ions such as N_3^-, OCN^-, and SCN^- in place of traditional halides. Azide (N_3^-) is particularly interesting as a low-cost and low-molecular weight ion that also adds a functional handle for further modification such as through N-atom-transfer or click chemistry, which have been demonstrated in many molecular examples and to a much more limited degree in the solid state.[21–26] Intriguingly, $BiON_3$ has been described in just a single report that only contains a general synthetic procedure—involving precipitation using $Bi(NO_3)_3{\cdot}5H_2O$ and NaN_3 in HNO_3, which presents potential hazards associated with evolution of HN_3—and discussion of vibrational spectroscopy of the $BiON_3$ product.[27] Detailed structural information, alternative synthetic approaches, and in-depth electronic and thermal behaviors remain unexplored. Herein, we report a study of the synthesis, structure, and thermal and electronic properties of $BiON_3$ and associated (pseudo)halide exchange reactions to provide a more comprehensive understanding of pseudohalide incorporation into

Department of Chemistry and Biochemistry, University of Notre Dame, Notre Dame, Indiana 46556, USA. E-mail: ajaffe@nd.edu

$[Bi_2O_2]^{2+}$ materials and to further develop avenues for functional modification of these promising compounds.

Synthetic approaches

Safety warning

Alkali azide salts and metal azides pose potential hazards associated with thermal instability, shock sensitivity, and/or the evolution of toxic HN_3 gas under acidic conditions. Discussion of safe standard operating procedures is available in the SI.

We explored three synthetic routes to isolate $BiON_3$ under relatively mild conditions (Fig. 1): post-synthetic exchange (PSE), solvothermal synthesis (ST), and coprecipitation (CP). In the post-synthetic exchange strategy, a BiOI precursor was synthesized *via* precipitation from $Bi(NO_{3)3}{\cdot}5H_2O$ and KI (Fig. S1).[28] BiOCl and BiOBr were synthesized through the reaction of Bi_2O_3 with the corresponding hydrohalic acid (Fig. S2), using conditions detailed in the SI. These bismuth oxyhalide precursors were then combined with aqueous NaN_3, followed by evaluation of reaction progress as a function of varying reactant molar ratios through powder X-ray diffraction (PXRD) and infrared (IR), Raman, and X-ray fluorescence (XRF) spectroscopies (Fig. S3–S13). With attempted exchange using a 1 : 10 ratio of BiOCl : NaN_3 (yielding PSE-BiOCl-10) or BiOBr : NaN_3 (yielding PSE-BiOBr-10), respectively, full conversion is not obtained (Fig. S3–S7). Instead, mixtures of the BiOX reactant and the desired product phases are observed. Re-reacting these partially converted samples with subsequent ten-fold excess of NaN_3 diminishes but does not eliminate remnant BiOX. Complete conversion of the BiOCl to $BiON_3$ is observed when an even larger excess of NaN_3 was utilized for the post-synthetic exchange reaction (PSE-BiOCl-100) (Fig. 2A–C, Fig. S8 and S9). To investigate if this exchange process is reversible, a mixed N_3^-/Cl^- sample synthesized through PSE at room temperature over seven days using a 1 : 50 ratio of BiOCl : NaN_3 (PSE-BiOCl-50) was exposed to 50-fold excess of NaCl, which yielded BiOCl (Fig. S8 and S9). Reacting PSE-BiOCl-50 with a 50-fold excess of NaN_3 shows further conversion to the $BiON_3$ product.

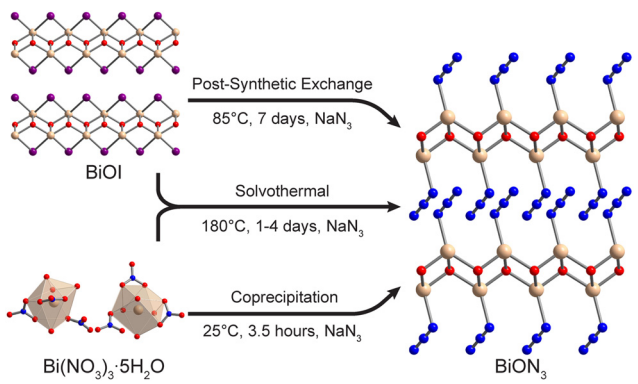

Fig. 1 Schematic of $BiON_3$ synthetic strategies. Bi, O, I, and N atoms are represented by tan, red, purple, and blue spheres, respectively. Disorder is omitted for clarity.

In contrast, when deriving materials from BiOI, PXRD suggests a single microcrystalline phase is obtained from the reaction of bismuth oxyiodide with NaN_3 in a 1 : 5 ratio (Fig. 2, Fig. S10). Given its more facile apparent anion exchange, the BiOI system was therefore utilized for further exchange studies to more deeply investigate potential solid-solution and/or doping behavior (Fig. S10–S13). Here, PSE reactions using BiOI : NaN_3 ratios of 1 : 1, 1 : 2, 1 : 5, 1 : 7, and 1 : 10 (Table S1) are denoted PSE-BiOI-1, PSE-BiOI-2, PSE-BiOI-5, PSE-BiOI-7, and PSE-BiOI-10, respectively. Diffraction patterns indicate that the lowest angle peak for BiOI at 9.81° 2θ—corresponding to the (001) reflection and indicative of the interlayer spacing—begins to shift to slightly higher angles with increasing concentration of NaN_3. Meanwhile, the (110) and (102) reflections at approximately 29.8° and 31.8°, respectively, attributed to the BiOI precursor, are still present after reacting with NaN_3 in a 1 : 1 ratio and disappear entirely in the PSE-BiOI-2, PSE-BiOI-5, PSE-BiOI-7, and PSE-BiOI-10 samples (Fig. S10). Additionally, after reaction with NaN_3 in a 1 : 2 ratio, the appearance of peaks at approximately 25.5°, 30.9°, 33.5°, and 35° 2θ further indicates formation of a new phase. Successful incorporation of the N_3^- into the BiOX structure is corroborated by vibrational spectroscopy (Fig. 2B and C, Fig. S11 and S12). Characteristic N_3^- peaks associated with asymmetric stretches (ν_{as}), symmetric stretches (ν_s), and bends (δ) are observed in IR and Raman spectra in all PSE samples *ca.* 2100 cm^{-1}, 1300 cm^{-1}, and 600 cm^{-1}, respectively (Fig. 2B and C), which are in agreement with the early report by Dehnicke.[27] We note that a weak lower-energy peak that we assign as an A_{1g} Bi–I mode (ν(Bi–I)) is observed in Raman spectra for PSE-BiOI-1 and PSE-BiOI-2 (Fig. S11) at approximately 90 cm^{-1}.[29,30] This suggests the presence of remnant I^-. Further, in IR spectra of PSE-BiOI-1, three peaks are observed at 1474, 1386, and 848 cm^{-1}, as well as two more in PSE-BiOI-2 at 1195 and 1019 cm^{-1} (Fig. S12). We attribute these features to modes associated with $(NO_x)^-$ species, though the complex speciation and wide-ranging binding motifs available for $(NO_x)^-$ make more detailed assignment challenging.[31] These peaks diminish in intensity for the PSE-BiOI-5 sample, and are not observed in PSE-BiOI-7 and PSE-BiOI-10, suggesting that with higher concentrations of NaN_3, the $(NO_x)^-$ species that presumably remain from the $Bi(NO_3)_3{\cdot}5H_2O$ precursor can be removed from the material.

We acquired X-ray fluorescence spectra to better assess residual I^- (Fig. S13, Table S2). These XRF spectra indicate that all PSE samples contain iodide in at least trace quantities, supporting the observation of Bi–I related peaks in their Raman spectra. Interestingly, PSE-BiOI-2 and PSE-BiOI-5 appear to have the least amount of I^-, while the 1 : 1 sample unsurprisingly has the highest concentration. Overall, while this analysis indicates that PSE is a viable method for incorporation of N_3^- in the $[Bi_2O_2]^{2+}$ slabs of BiOX, these exchanges are often incomplete, since Cl^-, Br^-, and I^- remain present in all samples despite their apparent phase purity in powder diffractograms. As discussed below, the continued presence of mixed anions has important implications for the optical and electronic behavior of these BiOX.

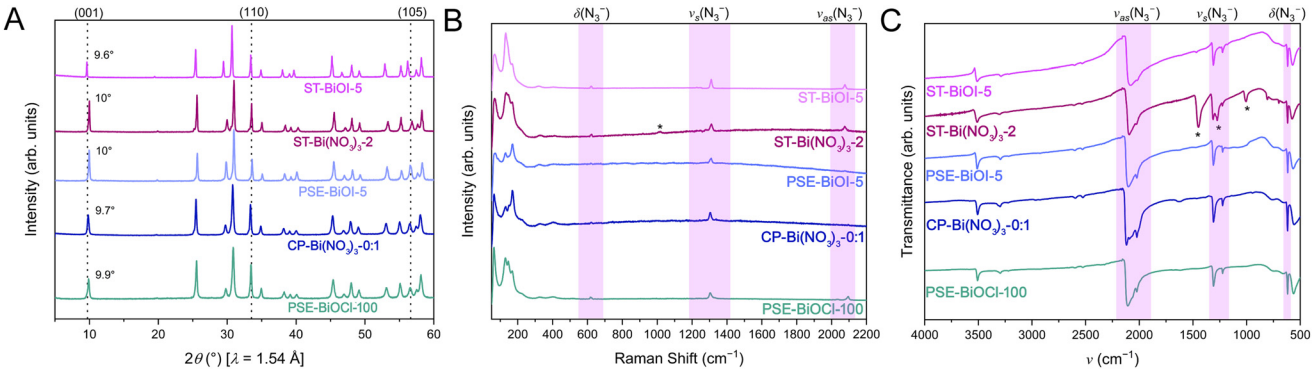

Fig. 2 Characterization of $BiON_3$ isolated through multiple synthetic strategies. (A) Powder X-ray diffraction patterns. For clarity, the (001), (110), and (105) reflections are labeled. (B) Raman spectra. The regions in which the ν_s, ν_{as}, and δ N_3^- modes appear are highlighted in pink. The asterisk denotes $(NO_x)^-$ species. (C) FT-IR spectra. Similarly, the regions in which the ν_s, ν_{as}, and δ N_3^- modes appear are highlighted in pink. Asterisks denote peaks that are attributed to the presence of $(NO_x)^-$ species.

We next explored solvothermal syntheses as an alternative route to the isolation of $BiON_3$. In our solvothermal approach, we compared the use of $Bi(NO_3)_3{\cdot}5H_2O$ and BiOI as bismuth-containing precursors, using NaN_3 as the azide source. When utilizing bismuth nitrate, reactant ratios of 1 : 1 (ST-$Bi(NO_3)_3$-1) and 1 : 2 (ST-$Bi(NO_3)_3$-2) were used, while BiOI and NaN_3 were combined in ratios of 1 : 2 (ST-BiOI-2) and 1 : 5 (ST-BiOI-5). Full synthetic details can be found in the SI. When using bismuth nitrate, the powder diffraction pattern of ST-$Bi(NO_3)_3$-1 shows a mixture of two phases (Fig. S14): the desired $BiON_3$ product and a reported orthorhombic $Bi_2O_2(OH)(NO_3)$ material.[32,33] In contrast, ST-$Bi(NO_3)_3$-2 appears to show full conversion to $BiON_3$ with no apparent reflections associated with $Bi_2O_2(OH)(NO_3)$. The $\nu_{as}(N_3^-)$ stretch is observable in IR spectra for both samples at 2090 cm^{-1} (Fig. S15). Similar peaks are also observed in the Raman spectra (Fig. S16). However, we note that the IR spectra also exhibit $(NO_x)^-$ peaks similar to those described above.[31] This suggests that while higher N_3^- concentrations result in more complete azide integration, the $(NO_x)^-$ ions may either be incorporated as heteroionic dopants or bind to particle surfaces.

Powder diffraction patterns from solvothermal reactions employing BiOI precursor (Fig. S17) indicate incomplete conversion from BiOI in ST-BiOI-2, as well as the appearance of new peaks at 28.8°, 36.2°, and 41.7° 2θ, that are not attributable to either the BiOI precursor or the desired $BiON_3$ product. However, diffraction analysis of ST-BiOI-5 corroborates more complete conversion to $BiON_3$ material (Fig. 2) and Raman and IR spectra support the incorporation of N_3^- (Fig. S18 and S19). Nevertheless, the Raman analysis of ST-BiOI-5 still shows the A_{1g} ν(Bi–I) mode at 88 cm^{-1}, implying that the $BiON_3$ product contains some I^-.[29,30] This residual iodide presence is corroborated by the XRF spectroscopy of the ST-BiOI-2 and ST-BiOI-5 samples (Table S3 and Fig. S20), where remnant iodide is observed in both samples. As expected, there is a higher content of iodide present in the ST-BiOI-2 sample: 22(9) atom percent compared to 3.0(6) atom percent for the ST-BiOI-5 sample. Analogous to a PSE approach, our investigation indicates that solvothermal syntheses represent a viable route to single-phase $BiON_3$ materials yet also leads to doping of heteroanionic species in the form of $(NO_x)^-$ and/or I^-.

We turned to coprecipitation for the isolation of $BiON_3$, as well as to provide finer control over the generation of potential solid solutions of the form $BiOI_xN_{3(1-x)}$. Here, $Bi(NO_3)_3{\cdot}5H_2O$ was combined with NaI and NaN_3 in ethylene glycol at room temperature for 4 h in NaI : NaN_3 ratios of 1 : 0, 0.75 : 0.25, 0.50 : 0.50, 0.25 : 0.75, and 0 : 1. Powder diffraction patterns of the 1 : 0 sample match the simulated pattern of BiOI (Fig. S21). In the 0.75 : 0.25 sample, a shift in the (102) reflection is observed from 29.7° in the BiOI phase to 29.1° in the new phase, indicating an increased interplanar *d*-spacing. This increase may be attributable to the incorporation of the larger N_3^- polyatomic anion into the structure. This observation coincides with an increase in the full-width-at-half-maximum (fwhm) of this peak from a value of 0.8 to 1.4, suggesting either a decrease in the crystallite domain size or strain/disorder being present in the sample.[34] Given that the neighboring (110) reflection shows little shifting and a constant fwhm value of 0.5 between the 0 : 1 and 0.75 : 0.25 samples, it is more probable that the behavior observed in the (102) reflection arises from microstrain and/or disorder rather than domain size increase. In the 0.50 : 0.50 sample, the (110) reflection begins to shift to higher angles, suggesting a decrease in the interplanar *d*-spacing. A similar shift is observed for the (200) reflection from 45° to 46° 2θ. Additionally, broadening is observed and is much more pronounced in this sample compared to the 1 : 0 and 0.75 : 0.25 samples, though some of this may be attributable to variation between instrumental peak profiles (see SI). The powder pattern of the 0.25 : 0.75 sample shows a loss in intensity of all previously observed reflections, signaling a loss in the crystallinity of the sample. Coinciding with this is the growth of new reflections consistent with the proposed $BiON_3$ phase. Combination of $Bi(NO_3)_3{\cdot}5H_2O$ and NaN_3 without BiOI (*i.e.*, the 0 : 1 sample) yields a powder pattern that is consistent with that observed for other $BiON_3$ samples without extraneous peaks (Fig. 2A).

Raman spectra of the 1 : 0 sample (Fig. S22) match BiOI synthesized *via* previous routes (see above), further indicating successful isolation of bismuth oxyiodide. In the 0.75 : 0.25 sample, there is a loss in intensity of the peak at 150 cm^{-1} assigned as the E_g mode, implying a lower amount of I^-. Further, with increasing concentration of NaN_3, we observed the growth of a peak at 158 cm^{-1}, which we assign as the growth of a ν(Bi–N) mode. Dehnicke reports similar peaks for AgN_3 and TiN_3, however no analogous peak was observed for $BiON_3$ in that report.[27] In the 1 : 0, 0.75 : 0.25, and 0.50 : 0.50 samples containing I^-, a peak assigned to the E_g ν(Bi–I) mode is observed at 151 cm^{-1}.[29,30] This ν(Bi–I) peak diminishes in intensity with increasing azide content. Curiously, while a peak attributed to the $\nu_{as}(N_3^-)$ mode is observed in the 0.75 : 0.25 and 0.50 : 0.50 samples at 2048 cm^{-1}, no $\nu_s(N_3^-)$ peak can be identified. Conversely, in the 0.25 : 75 and 0 : 1 sample, only the peak corresponding to $\nu_s(N_3^-)$ is observed at 1334 cm^{-1} and 1304 cm^{-1}, respectively. This may suggest that bulk symmetry changes associated with an increasing concentration of N_3^- and decreasing concentration of I^- within the lattice are responsible for determining which vibrational peaks are symmetry-allowed, but this warrants further investigation. The IR and Raman spectra for the 0 : 1 sample show no evidence of the previously observed $(NO_x)^-$ peaks (Fig. 2B, S22). The incorporation of iodide in the coprecipitated samples was further corroborated by XRF and IR spectroscopies (Fig. S23 and S24, Table S4). In XRF spectroscopy, it is observed that the $L_{\alpha 1}$ and $L_{\beta 1}$ peaks associated with iodine decrease in intensity with increasing equivalents of NaN_3 being used in the reaction. Supporting evidence from the IR spectra of the samples confirms the presence of ν_{as} N_3^- modes at approximately 2040 cm^{-1} in the 0.75 : 0.25, 0.50 : 0.50, 0.25 : 0.75, and 0 : 1 samples. We surmise that the loss of iodide observed by XRF is due to the successful incorporation of N_3^- into the materials. Coprecipitation therefore represents an intriguing approach to the isolation of new bismuth oxypseudohalides, while precluding their doping with remnant heteranions. It also allows for finer control of anion ratios in mixed-anion systems.

Structural analysis

To elucidate how N_3^- ions are oriented between the $[Bi_2O_2]^{2+}$ slabs, we carried out Rietveld refinement using powder diffraction data collected for the coprecipitated $BiON_3$ sample (without the presence of an iodide source) to yield the first structural description of $BiON_3$ (Fig. 3, Tables S5–S7, see SI for refinement details). After collecting diffraction data from 5–100° 2θ, the powder pattern was indexed using N-TREOR09 implemented in EXPO2014.[35,36] Two plausible space groups were determined: $P4/n$ and $P4/nmm$. Since $BiON_3$ is adequately modelled using the higher-symmetry tetragonal $P4/nmm$ space group, and further, this is the reported space group for other bismuth oxyhalides, we selected this space group for further refinement. Rietveld refinement yields lattice parameters of

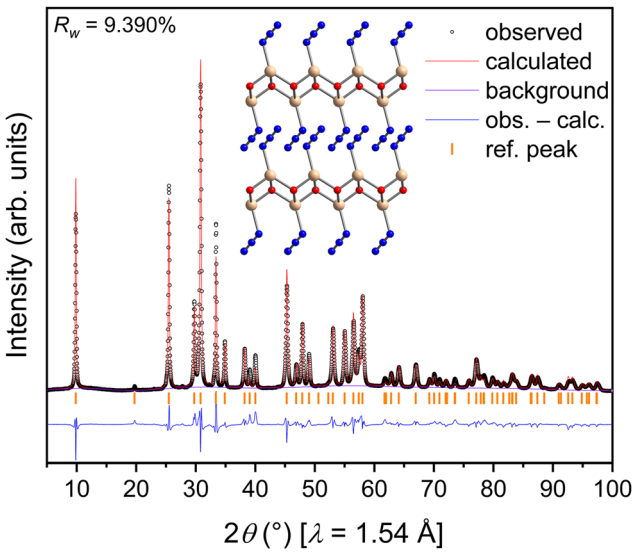

Fig. 3 Rietveld refinement performed on $BiON_3$ synthesized *via* coprecipitation. Symmetry-related disorder of Bi and N atoms is omitted for clarity.

$a = b = 3.79812(8)$ Å and $c = 9.01606(23)$ Å, with a unit cell volume of 130.063(5) $Å^3$ (Table S5). In our initial model, the bismuth and azide nitrogen atoms were located at high-symmetry special positions with respect to their x and y coordinates. However, examination of calculated *vs.* observed reflection intensities (Fig. S25), refinement statistics, and unmodeled electron density within Fourier difference maps (Fig. S26 and S27) suggests that the bismuth centers and nitrogen atoms may exhibit symmetry-related disorder (Fig. S26A, S26D, and S27A). Moving the Bi atoms off their special positions—also reducing their site occupancies to maintain the $BiON_3$ formula—and allowing their coordinates to refine freely improves the fit (Fig. S28) and electron density modelling (Fig. S26B, S26E, and S27B). However, disagreement between calculated and observed intensity at certain reflections (*e.g.*, 29° 2θ) persists, additional minor unmodelled electron density is observed, and the azide atoms' isotropic thermal displacement parameters, U_{iso}, refine to large values, similarly indicating the potential for disorder. Moving the azide N atoms from their special positions in a similar manner to the Bi atom yields substantial further improvement in the fit (Fig. 3, Fig. S26C, S26F, and S27C). As such, the nitrogen and bismuth atomic positions were then allowed to refine freely, along with isotropic displacement parameters for all atoms. The oxygen atoms remain on special positions. In addition to refinement of particle size and strain,[37] we note that preferred orientation was modelled using spherical harmonics, since a pattern collected on an instrument in a Debye-Scherrer geometry using sample rotation—though of insufficient resolution for Rietveld—shows more similar relative peak intensities to the model's simulated pattern (Fig. S29). Full discussion of the refinement is available in the SI. The final refinement (Fig. 3) resulted in adequate fit with R_w = 9.390% (Table S5). The refined model

suggests that the azide binds in a tilted, end-on fashion, and both this molecular unit and the Bi centers feature symmetry-related disorder about the four-fold axis.

In the structure of $BiON_3$, we note the average Bi–O–Bi angle of 110(3)° is almost the same as 114.015(134)° for BiOCl, though more acute than in BiOI (117.93°).[38,39] Such changes may manifest in altered orbital overlap, thereby tuning electronic band structure. The closest Bi–N distance is 2.6928(1) Å for the terminally bound, disordered azide. However, we note that the pendant nitrogen atom on the other end of the azide ion is relatively close to the bismuth atoms of the adjacent layer, with a distance of 3.54820(5) Å to the nearest Bi while also sitting in a position that would bridge between four equivalent Bi sites if the azide was not tilted. This distance is slightly larger than the Bi–I distance of approximately 3.38 Å in BiOI.[39] The closer approach of the azide ion to the $[Bi_2O_2]^{2+}$ slabs and overall different binding mode when compared to BiOCl (3.0678(35) Å)[38] again may ultimately impact the electronic structure of the compound, such as by increasing participation of azide states within bonding and antibonding interactions.

Electronic property tuning

The introduction of new ions into the $[Bi_2O_2]^{2+}$ slabs should have a significant effect on the band structure and subsequently the electronic properties of these materials, as described above. Specifically, the valence band of bismuth oxy(pseudo)halide materials is primarily derived from (pseudo) halide p orbitals along with bismuth 6s and O 2p orbitals, whereas the conduction band is primarily comprised of bismuth 6p orbitals.[7,8,40,41] As a function of this electronic structure, experimentally determined band gaps decrease from 3.22–3.37 to 2.64–2.82 to 1.77–1.95 eV within the series of BiOCl, BiOBr, and BiOI, respectively,[13,42–44] due to the introduction of higher-energy halide p orbitals that elevate the valence band maximum.[6,8] We hypothesized the substitution of azide-based nitrogen 2p orbitals and removal of halogen p orbitals would provide an avenue for band gap tuning, as would changes in orbital overlap as a function of interatomic distances.[6] Therefore, we sought to monitor changes in these materials' band gaps as they relate to the identity and concentration of the ions incorporated to ultimately provide guiding principles for their future optoelectronic tuning. Diffuse reflectance ultraviolet–visible spectra were acquired for $BiON_3$ samples synthesized through the PSE, solvothermal, and coprecipitation methods. Transformation of the diffuse reflectance data using the Kubelka–Munk equation yields spectra in the form of α/S *vs.* energy, where α is the absorption coefficient and S is the scattering coefficient.[45,46] Band gaps can be calculated *via* linear extrapolation from these plots—the Tauc method of plotting $(\alpha h\nu)^2$ *vs.* $h\nu$ or $(\alpha h\nu)^{1/2}$ *vs.* $h\nu$ for direct-gap or indirect-gap semiconductors, respectively, is not appropriate given two-dimensional materials' lack of energy-dependence for their density of states at the band edge (see SI for discussion).[47,48]

In agreement with prior reports,[49] we observe that band gap decreases with increasing principal quantum number within the halide series (Fig. 4): BiOCl, BiOBr, and BiOI exhibit band gaps of 3.54(1), 2.90(1), and 2.21(1) eV, respectively. We note that this BiOI—synthesized *via* coprecipitation from bismuth nitrate and KI—displays a slightly larger apparent band gap than the 1.77–1.95 eV gap that is described in some literature reports,[2,13,28] although we do observe a small degree of absorption below the absorption edge—closer to 1.95 eV and therefore more similar to previous work. While some of this difference may also be attributable to differences in how band gap values are experimentally determined (see SI for discussion), we attribute this larger band gap to the presence of the trace $(NO_x)^-$ that presumably comes from the bismuth nitrate precursor. Indeed, materials such as the BiOI-derived post-synthetic exchange sample PSE-BiOI-1 and the solvothermally synthesized ST-BiOI-2 feature lower absorption onsets of 2.05(4) eV (Fig. S30) and 2.08(2) eV (Fig. S31), respectively, that are much more similar to the literature-reported band gap for BiOI. In both cases, our earlier analysis showed remnant BiOI from the incomplete conversion to $BiON_3$, corroborated here by additional potential absorption onsets at higher energy that suggest a biphasic mixture. We therefore suggest that the additional reaction steps may allow for removal of $(NO_x)^-$ from this remaining BiOI, thereby lowering the observed absorption onset closer to the reported value. This provides an early indicator of the substantial effects that even minor heteroanion inclusion have on the materials' electronic structures (Fig. 4, Fig. S30–S33; Table S8).

Bismuth oxyazide samples synthesized from oxyhalide precursors further exemplify the important effects of anion substitution. For example, $BiON_3$ acquired *via* PSE on BiOCl exhibits a lower band edge than BiOCl: its band gap *ca.* 3.37(1) eV is approximately 150 meV lower than the band gap of BiOCl

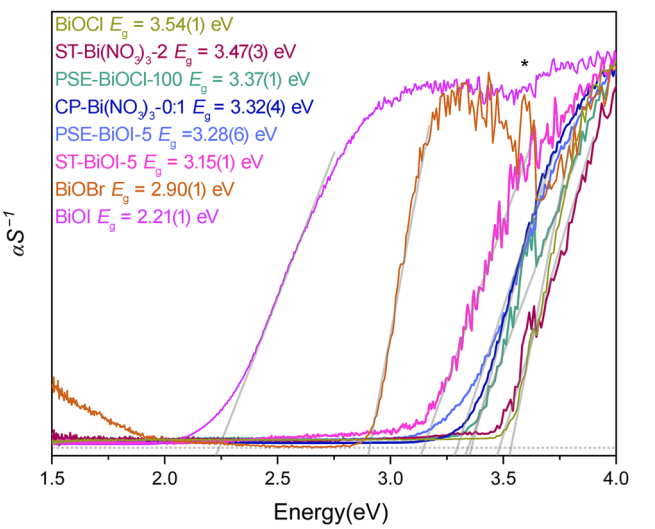

Fig. 4 Diffuse reflectance spectra of $BiON_3$ isolated *via* multiple methods, shown in comparison to BiOCl, BiOBr, and BiOI. The asterisks denote an artifact resulting from a bulb changeover.

(Fig. 4). Though the foregoing results suggest that some Cl^- remains in the system, this implies the valence band behavior is largely dictated by azide states. Compounds derived from BiOI, such as PSE-BiOI-2, PSE-BiOI-5, PSE-BiOI-10, and the solvothermally synthesized ST-BiOI-5 show similar though slightly smaller band gaps of 3.23(6) eV, 3.28(6) eV, 3.21(8) eV, and 3.15(1) eV, respectively (Fig. S30–S31). These values suggest that in each case, N_3^- dominates valence band behavior, though trace I^- may mildly elevate the valence band. The PSE-BiOI-7 has an anomalously small band gap of 3.07(5) eV. One potential explanation is an intermediate concentration of both I^- and N_3^- leading to cooperative effects: (a) the greater electronegativity of the azide may lower the Bi-derived conduction band edge position while (b) the higher energies of I 5p orbitals raise the valence band maximum. Alternatively, the presence of some pre-edge absorption, *i.e.*, Urbach tails, in the PSE-BiOI-7 and PSE-BiOI-10 samples may suggest the presence of mid-gap defect states.[50] UV–visible spectra of $BiON_3$ samples that contain $(NO_x)^-$, such as ST-Bi$(NO_3)_3$-1 and ST-Bi$(NO_3)_3$-2, show band gaps of 3.396(2) and 3.47(3) eV (Fig. 4, Fig. S32). Since $Bi_2O_2(OH)(NO_3)$ has a reported band gap of between 3.17–3.25 eV,[41,51] these larger band gaps may similarly arise due to simultaneous effects from $(NO_x)^-$ and N_3^- that cooperatively widen the gap. Finally, when considering the $BiO(N_3)_{1-x}I_x$ samples synthesized *via* coprecipitation, an expected increase in band gap is observed with increasing N_3^- content (Fig. S33, Table S8). The trend is consistent with valence band behavior being dominated by I^- 5p states at low N_3^- concentration and by N_3^- states at high azide concentration, thereby raising the valence band maximum. Overall, across the different methods employed to synthesize $BiON_3$, the band gaps remain similar though the inclusion of heteroanionic species allows for a "tuning knob" to vary this value.

Temperature-induced evolution

To our knowledge, the thermal behavior of $BiON_3$ has not been studied, yet its investigation can point to its synthetic utility to form new potential species: the thermolysis of N_3^- features entropic and enthalpic driving forces to break the N–N bond to form N_2 and possible nitride species. This so called atom-transfer has not be well explored in solid-state systems, though synthesis of metal nitrides through presumed metal azide precursors has been reported *via* solvothermal methods.[22] We carried out thermogravimetric analysis coupled to differential scanning calorimetry (TGA-DSC) as well as thermolysis experiments under oxidative and inert atmospheres. The TGA-DSC data for $BiON_3$ shows a distinct two-step feature between 200 °C and 400 °C (Fig. 5), corresponding to a mass loss of 11%. This two-step mass loss also corresponds to two exothermic events. Another mass loss event of 1.1% is observed between 400 °C and 500 °C, accompanied by an endothermic event centered at approximately 400 °C.

To further elucidate this thermal decomposition behavior, we conducted thermolysis experiments on $BiON_3$ in both inert and aerobic atmospheres (Fig. S34–S37). Thermolysis in air was carried out in a box furnace within an alumina crucible, heating overnight at 200 °C, 300 °C, and 450 °C, respectively. The powder diffraction pattern of the sample heated to 200 °C (PSE-BiOCl-100 @200 °C) indicates retention of the $BiON_3$ phase (Fig. S34), but the wider diffraction peaks suggest decreased crystallinity: the fwhm of the (001) reflection increases from 0.31° to 0.68° 2θ from the $BiON_3$ to the PSE-BiOCl-100 @200 °C sample, respectively. The sample thermolyzed at 300 °C (PSE-BiOCl-100 @300 °C), indicates new reflections at 23.8°, 28.7°, 32.3°, and 46.5° 2θ and loss of all reflections attributed to the $BiON_3$ material. The new reflections are broader than those of the $BiON_3$ and PSE-BiOCl-100 @200 °C samples, with fwhm values of 0.75°, 1.6°, 0.78°, and 1.3° 2θ, consistent with reduced crystallinity. Finally, the powder pattern of the material heated at 450 °C (PSE-BiOCl-100 @450 °C) matches the simulated pattern of α-Bi_2O_3—though non-crystalline phases may also be present—confirming loss of N_3^- and subsequent oxidation by O_2.[52]

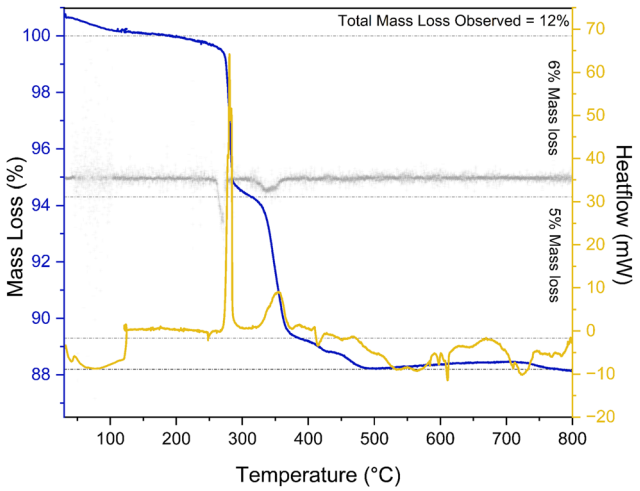

Fig. 5 TGA (blue) and DSC (yellow) traces for PSE-BiOCl-100. The gray trace indicates the first derivative of the mass loss. N_2 flow gas was used for this experiment, with a heating rate of 1 °C min^{-1}.

Infrared spectroscopy was utilized to track loss of azide and appearance of new potential Bi–N related peaks in the aerobically heat-treated samples (Fig. S35). FT-IR spectra of the PSE-BiOCl-100 @200 °C sample display all N_3^--related peaks observed in the $BiON_3$ starting material, though a small change in the $\nu_{as}(N_3^-)$ peak profile is observable. In PSE-BiOCl-100 @300 °C samples, the $\nu_s(N_3^-)$ peak disappears and the $\nu_{as}(N_3^-)$ peak at 2048 cm^{-1} decreases in intensity. It is interesting to note that the higher-energy $\nu_{as}(N_3^-)$ peak red shifts from 2105 cm^{-1} at room temperature to 2065 cm^{-1} and 2048 cm^{-1} upon heating to 200 °C and 300 °C, respectively. This suggests a large potential change in the chemical environment of the azide. Additionally, the appearance of peaks at 1445 cm^{-1}, 1324 cm^{-1}, 1048 cm^{-1}, and 852 cm^{-1} in PSE-BiOCl-100 @300 °C is consistent with the formation of $(NO_x)^-$ species. Subsequently, in PSE-BiOCl-100 @450 °C, we

observe the complete disappearance of $\nu_{as}(N_3^-)$ peaks, suggesting full loss of the azide. The previously observed peaks attributed to the formation of $(NO_x)^-$ in the PSE-BiOCl-100 @300 °C are also present in the PSE-BiOCl-100 @450 °C sample. These peaks shift to 1455 cm^{-1}, 1388 cm^{-1}, and 845 cm^{-1} and grow in intensity. Finally, we observe peaks at approximately 1630 cm^{-1} in PSE-BiOCl-100 @200 °C and PSE-BiOCl-100 @300 °C that we attribute to water, likely adsorbed from the atmosphere. In the PSE-BiOCl-100 @450 °C sample, the peak at approximately 1630 cm^{-1} is absent, in agreement with the relatively low hygroscopicity of α-Bi_2O_3.

To gain a better understanding of the decomposition products under inert conditions, thermolysis under argon atmosphere was conducted at 320 °C (PSE-BiOCl-100 @320 °C) in a glovebox. The resulting solid was then isolated and measured under air-free conditions using a capillary. Interestingly, PXRD patterns (Fig. S36) show the appearance of peaks that are consistent with elemental Bi, suggesting reduction of the bismuth centers under inert conditions.[53] Reduction of BiOCl by NaN_3 decomposition has been reported as means of forming oxygen vacancies and subsequently improving photocatalytic performance.[54] Additionally, there have been reports of formation of catalytically active elemental Bi with exposed (003) facets *via* the electrochemical reduction of BiOX materials.[55] However, the mechanism of reduction in our system remains to be determined, including the nature of the accompanying oxidized species and whether any amorphous phases are produced. When the thermolyzed product is exposed to an oxidative atmosphere, a mixture of phases appears, as indicated by two sets of reflections, some sharp and some broader. The sharp reflections observed at 23.4°, 24.9°, 33.5°, 38.0°, and 48.4° 2θ have not yet been assigned. The second phase shows peaks at 28.4°, 32.6°, 47°, and 55° 2θ and are similar to those observed in the PSE-BiOCl-100 @300 °C sample. They may potentially be attributed to formation of the metastable β-Bi_2O_3.[56] The IR spectrum of the PSE-BiOCl-100 @320 °C sample exhibits a $\nu_{as}(N_3^-)$ peak, indicating azide is still present in the sample after heating at 320 °C. This is consistent with the mass losses observed in the TGA-DSC, which suggest that at this temperature, only half of the azide molecules have decomposed. The IR spectra of the thermolyzed sample after exposure to air shows the growth of four peaks at 849 cm^{-1}, 1041 cm^{-1}, 1323 cm^{-1}, and 1438 cm^{-1}, which we attribute to $(NO_x)^-$ formation (Fig. S37). It is worth noting that these peaks were not observed in sample heated to 320 °C that was stored in the glovebox and are consistent with peaks observed in PSE-BiOCl-100 @300 °C sample.

Conclusions

Herein, we have developed synthetic approaches for $BiON_3$—an unexplored BiOX material—through three routes: post-synthetic exchange using azide salts, hydrothermal synthesis *via* a bismuth nitrate or BiOI precursor, and coprecipitation. We have demonstrated that these approaches provide a means of modifying the electronic behavior of layered bismuth oxy(pseudo)halide materials through formation of apparent mixed-anion solid solutions and/or low-concentration heteroanionic doping. Further, we have determined the structure of $BiON_3$ crystallographically for the first time. Rietveld refinement suggests the N_3^- ion is oriented in a tilted, end-on fashion disordered over four positions and bound to a four-fold-disordered bismuth center, while also in proximity to bismuth atoms of the adjacent layer. The pendant azides are therefore interdigitated between $[Bi_2O_2]^{2+}$ slabs. Exploration of the thermal response of $BiON_3$ has then revealed intriguing reactivity to related to N_3^- loss, which results in reduction to elemental Bi under inert atmosphere. Investigation of samples thermolyzed in an inert atmosphere and exposed to air suggests the formation of $(NO_x)^-$ species, yielding promising implications for further modification of the material through nitrogen atom-transfer. This potentially offers a new synthetic route to mixed anion oxide and nitride materials that have been documented as promising battery electrode materials and electrocatalysts for ammonia formation.[57,58] Overall, pseudohalide incorporation into BiOX is a promising new frontier for the tuning of $[Bi_2O_2]^{2+}$-based materials that can enable their future implementation in photocatalysis, nonlinear optics, and optoelectronics.

Conflicts of interest

There are no conflicts to declare.

Data availability

The data supporting this article have been included as part of the SI. Supplementary information: experimental details, diffraction patterns, spectra, and supplemental discussion. See DOI: **https://doi.org/10.1039/d5qi01602a**.

Acknowledgements

Acknowledgement is made to the donors of the American Chemical Society Petroleum Research Fund for partial support of this research through PRF# 65120-DNI10. We thank The National GEM Consortium for support of A. E. P. through the GEM Fellowship. X-ray diffraction studies were carried out at the Notre Dame Molecular Structure Facility. We thank the ND Energy Materials Characterization Facility (MCF) for the use of the UV–Visible spectrometer to acquire diffuse reflectance measurements. The MCF is supported by Notre Dame Research. We thank Dr Allen Oliver for assistance with X-ray diffraction studies. We thank Prof. Annalise Maughan from the Colorado School of Mines for helpful discussions for powder X-ray diffraction refinements.

References

1 N. Tian, C. Hu, J. Wang, Y. Zhang, T. Ma and H. Huang, Layered bismuth-based photocatalysts, *Coord. Chem. Rev.*, 2022, **463**, 214515.

2 X. Zhang and L. Zhang, Electronic and Band Structure Tuning of Ternary Semiconductor Photocatalysts by Self Doping: The Case of BiOI, *J. Phys. Chem. C*, 2010, **144**, 18198–18206.

3 N. Ni, H. Li, L. He, J. Zhou, Z. Sang, Y. Liu, S. du, Q. Wang and Y. Tong, Structures and photocatalytic activities of bismuth oxyhalides nanoparticles developed by utilizing a simple reaction, *Mater. Sci. Eng., B*, 2022, **286**, 116031.

4 Z. Saddique, M. Imran, A. Javaid, S. Latif, N. Hussain, P. Kowal and G. Boczkaj, Band engineering of BiOBr based materials for photocatalytic wastewater treatment via advanced oxidation processes (AOPs) – A review, *Water Resour. Ind.*, 2023, **29**, 100211.

5 A. Parida, S. Senapati and R. Naik, Recent developments on Bi-based oxychalcogenide materials with thermoelectric and optoelectronic applications: an overview, *Mater. Today Chem.*, 2022, **26**, 101149.

6 D. Kato, H. Suzuki, R. Abe and H. Kageyama, Band engineering of layered oxyhalide photocatalysts for visible-light water splitting, *Chem. Sci.*, 2024, **15**, 11719–11736.

7 T. L. Wakjira, K. Tadele, A. B. Gemta and G. B. Kassahun, Electronic, optical, phonon, and thermodynamic properties of bismuth oxyhalides for photocatalysis application using density functional theory, *Discover Mater.*, 2024, **4**, 56.

8 A. M. Ganose, M. Cuff, K. T. Butler, A. Walsh and D. O. Scanlon, Interplay of Orbital and Relativistic Effects in Bismuth Oxyhalides: BiOF, BiOCl, BiOBr, and BiOI, *Chem. Mater.*, 2016, **28**, 1980–1984.

9 J. Li, Y. Yu and L. Zhang, Bismuth oxyhalide nanomaterials: layered structures meet photocatalysis, *Nanoscale*, 2014, **6**, 8473–8488.

10 L. Jia, D. Cui, J. Wu, H. Feng, Y. Yang, T. Yang, Y. Qu, Y. Du, W. Hao, B. Jia and D. J. Moss, Highly nonlinear BiOBr nanoflakes for hybrid integrated photonics, *APL Photonics*, 2019, **4**, 090802.

11 J. Jiang, K. Zhao, X. Xiao and L. Zhang, Synthesis and facet-dependent photoreactivity of BiOCl single-crystalline nanosheets, *J. Am. Chem. Soc.*, 2012, **134**, 4473–4476.

12 M. Pan, H. Zhang, G. Gao, L. Liu and W. Chen, Facet-dependent catalytic activity of nanosheet-assembled bismuth oxyiodide microspheres in degradation of bisphenol A, *Environ. Sci. Technol.*, 2015, **49**, 6240–6248.

13 Z. Jiang, X. Liang, Y. Liu, T. Jing, Z. Wang, X. Zhang, X. Qin, Y. Dai and B. Huang, Enhancing visible light photocatalytic degradation performance and bactericidal activity of BiOI via ultrathin-layer structure, *Appl. Catal., B*, 2017, **211**, 252–257.

14 X. He, J. Diao, Q. Yao, H. Wang, X. Zhong, W. Si, Q. Fu, L. Yuan, X. Zhang and Y. Xie, Activating Intrinsic Self-Trapped Exciton Emission in Bismuth Oxyhalides by Edge Iodine Doping, *ACS Photonics*, 2024, **12**, 384–391.

15 K. Sridharan, S. Shenoy, S. G. Kumar, C. Terashima, A. Fujishima and S. Pitchaimuthu, Advanced Two-Dimensional Heterojunction Photocatalysts of Stoichiometric and Non-Stoichiometric Bismuth Oxyhalides with Graphitic Carbon Nitride for Sustainable Energy and Environmental Applications, *Catalysts*, 2021, **11**, 426.

16 E. Johnson, A. Raj, S. Kottarathil, A. Johansson and K. Sridharan, Bismuth-rich $Bi_4O_5Br_2$ anchored on g-C_3N_4 nanosheets: Enhanced visible-light performance for simultaneous photocatalytic degradation of emerging pollutants and spectroscopic insights, *Sep. Purif. Technol.*, 2025, **364**, 132521.

17 J. Ma, J. Yan, J. Xu, J. Ni, H. Zhang and L. Lu, Dynamic ion exchange engineering BiOI-derived $Bi_2O_2CO_3$ to promote CO_2 electroreduction for efficient formate production, *Chem. Eng. J.*, 2023, **455**, 140926.

18 A. J. Corkett, Z. Chen, D. Bogdanovski, A. Slabon and R. Dronskowski, Band Gap Tuning in Bismuth Oxide Carbodiimide Bi_2O_2NCN, *Inorg. Chem.*, 2019, **58**, 6467–6473.

19 F. Reifler, H.-R. Oswald, R. A. Gubser, C. Baelocher and A. Reller, Synthesis, structure und thermochemical reactivity of bismuth methoxide, $BiOOCH_3$, *Solid State Ionics*, 1996, **84**, 283–291.

20 X. Zhang, Y. Liu, G. Zhang, Y. Wang, H. Zhang and F. Huang, Thermal decomposition of bismuth oxysulfide from photoelectric Bi_2O_2S to superconducting $Bi_4O_4S_3$, *ACS Appl. Mater. Interfaces*, 2015, **7**, 4442–4448.

21 M. Reiners, M. Maekawa, C. G. Daniliuc, M. Freytag, P. G. Jones, P. S. White, J. Hohenberger, J. Sutter, K. Meyer, L. Maron and M. D. Walter, Reactivity studies on [Cp'Fe(μ-I)]$_2$: nitrido-, sulfido- and diselenide iron complexes derived from pseudohalide activation, *Chem. Sci.*, 2017, **8**, 4108–4122.

22 J. Choi and E. G. Gillan, Solvothermal Metal Azide Decomposition Routes to Nanocrystalline Metastable Nickel, Iron, and Manganese Nitrides, *Inorg. Chem.*, 2009, **48**, 4470–4477.

23 H. C. Kolb, M. G. Finn and K. B. Sharpless, Click Chemistry: Diverse Chemical Function from a Few Good Reactions, *Angew. Chem., Int. Ed.*, 2001, **40**, 2004–2021.

24 E. M. Sletten and C. R. Bertozzi, Bioorthogonal chemistry: fishing for selectivity in a sea of functionality, *Angew. Chem., Int. Ed.*, 2009, **48**, 6974–6998.

25 M. Weidemann, D. Werhahn, C. Mayer, S. Klager, C. Ritter, P. Manuel, J. P. Attfield and S. D. Kloss, High-pressure synthesis of Ruddlesden-Popper nitrides, *Nat. Chem.*, 2024, **16**, 1723–1731.

26 P. Gray, Chemistry of the Inorganic Azides, *Q. Rev., Chem. Soc.*, 1963, **17**, 441–473.

27 K. Dehnicke, IR- und RAMAN-Spektren von CuN_3, AgN_3, TlN_3, $BiON_3$, $Cu(N_3)_2$ und α-$Pb(N_3)_2$, *Z. Anorg. Allg. Chem.*, 1974, **409**, 311–319.

28 X. Xiao and W.-D. Zhang, Facile synthesis of nanostructured BiOI microspheres with high visible light-

induced photocatalytic activity, *J. Mater. Chem.*, 2010, **20**, 5866–5870.
29 J. E. D. Davies, Solid State Vibrational Spectroscopy–III[1] The Infrared and Raman Spectra of The Bismuth(III) Oxide Halides, *J. Inorg. Nucl. Chem.*, 1973, **35**, 1531–1534.
30 H. H. Yang, K.-Y. Hsiao, F.-Y. Liu, C.-C. Chen and I. C. Chen, Vibrational Structures of Iodine-Vacancy Bismuth Oxyiodides Using Temperature-Dependent Low-Wavenumber Raman Spectroscopy, *J. Phys. Chem. C*, 2023, **128**, 563–570.
31 K. Nakamoto, *Infrared and Raman Spectra of Inorganic and Coordination Compounds, Part B. Applications in Coordination, Organometallic, and Bioinorganic Chemistry*, Wiley Interscience, 6 edn, 2009.
32 N. Henry, M. Evain, P. Deniard, S. Jobic, F. Abraham and O. Mentré, $[Bi_2O_2]^{2+}$ Layers in $Bi_2O_2(OH)(NO_3)$: Synthesis and Structure Determination, *Z. Naturforsch., B:J. Chem. Sci.*, 2005, **60**, 322–327.
33 M. Weil, O. P. Missen and S. J. Mills, Dimorphism of $[Bi_2O_2(OH)][(NO_3)$ - the ordered $Pna2_1$ structure at 100 K, *Acta Crystallogr.*, 2023, **79**, 1223–1227.
34 P. Scardi, Diffraction Line Profiles in the Rietveld Method, *Cryst. Growth Des.*, 2020, **20**, 6903–6916.
35 A. Altomare, G. Campi, C. Cuocci, L. Eriksson, C. Giacovazzo, A. Moliterni, R. Rizzi and P.-E. Werner, Advances in powder diffraction pattern indexing: N-TREOR09, *J. Appl. Crystallogr.*, 2009, **42**, 768–775.
36 A. Altomare, M. C. Burla, M. Camalli, B. Carrozzini, G. L. Cascarano, C. Giacovazzo, A. Guagliardi, A. G. G. Moliterni, G. Polidori and R. Rizzi, EXPO: a program for full powder pattern decomposition and crystal structure solution, *J. Appl. Crystallogr.*, 1999, **32**, 339–340.
37 W. Huo, W. Xu, Z. Guo, Y. Zhang and F. Dong, Motivated surface reaction thermodynamics on the bismuth oxyhalides with lattice strain for enhanced photocatalytic NO oxidation, *Appl. Catal., B*, 2021, **284**, 119694.
38 P. Halappa, H. M. Rajashekar and C. Shivakumara, Synthesis and structural characterization of orange red light emitting Sm^{3+} activated BiOCl phosphor for WLEDs applications, *J. Alloys Compd.*, 2019, **785**, 169–177.
39 F. A. Bannister, The crystal-structure of the bismuth oxyhalides, *Mineral. Mag. J. Mineral. Soc. (1876–1968)*, 1935, **24**, 49–58.
40 Z. Y. Zhao, Q. L. Liu and W. W. Dai, Structural, Electronic, and Optical Properties of $BiOX_{1-x}Y_x$(X, Y = F, Cl, Br, and I) Solid Solutions from DFT Calculations, *Sci. Rep.*, 2016, **6**, 31449.
41 H. Huang, Y. He, X. Li, M. Li, C. Zeng, F. Dong, X. Du, T. Zhang and Y. Zhang, $Bi_2O_2(OH)(NO_3)$ as a desirable $[Bi_2O_2]^{2+}$layered photocatalyst: strong intrinsic polarity, rational band structure and {001} active facets co-beneficial for robust photooxidation capability, *J. Mater. Chem. A*, 2015, **3**, 24547–24556.
42 H. Feng, Z. Xu, L. Wang, Y. Yu, D. Mitchell, D. Cui, X. Xu, J. Shi, T. Sannomiya, Y. Du, W. Hao and S. X. Dou, Modulation of Photocatalytic Properties by Strain in 2D BiOBr Nanosheets, *ACS Appl. Mater. Interfaces*, 2015, **7**, 27592–27596.
43 J. Lv, Q. Hu, C. Cao and Y. Zhao, Modulation of valence band maximum edge and photocatalytic activity of BiOX by incorporation of halides, *Chemosphere*, 2018, **191**, 427–437.
44 S. Wang, D. Song, L. Liao, M. Li, Z. Li and W. Zhou, Surface and interface engineering of BiOCl nanomaterials and their photocatalytic applications, *Adv. Colloid Interface Sci.*, 2024, **324**, 103088.
45 P. Makula, M. Pacia and W. Macyk, How To Correctly Determine the Band Gap Energy of Modified Semiconductor Photocatalysts Based on UV-Vis Spectra, *J. Phys. Chem. Lett.*, 2018, **9**, 6814–6817.
46 P. Kubelka and F. Munk, Ein Beitrag Zur Optik Der Farbanstriche, *Z. Tech. Phys.*, 1931, **12**, 593–601.
47 J. Tauc, Optical Properties and Electronic Structure of Amorphous Ge And Si, *Mater. Res. Bull.*, 1968, **3**, 37–46.
48 J. Klein, L. Kampermann, B. Mockenhaupt, M. Behrens, J. Strunk and G. Bacher, Limitations of the Tauc Plot Method, *Adv. Funct. Mater.*, 2023, **33**, 2304523.
49 H. Cheng, B. Huang and Y. Dai, Engineering BiOX (X = Cl, Br, I) nanostructures for highly efficient photocatalytic applications, *Nanoscale*, 2014, **6**, 2009–2026.
50 S. Aljishi, J. D. Cohen, S. Jin and L. Ley, Band tails in hydrogenated amorphous silicon and silicon-germanium alloys, *Phys. Rev. Lett.*, 1990, **64**, 2811–2814.
51 L. Hao, H. Huang, Y. Guo and Y. Zhang, Multifunctional $Bi_2O_2(OH)(NO_3)$ Nanosheets with {001} Active Exposing Facets: Efficient Photocatalysis, Dye-Sensitization, and Piezoelectric-Catalysis, *ACS Sustainable Chem. Eng.*, 2018, **6**, 1848–1862.
52 Y. Astuti, A. Fauziyah, S. Nurhayati, A. D. Wulansari, R. Andianingrum, A. R. Hakim and G. Bhaduri, Synthesis of α-Bismuth oxide using solution combustion method and its photocatalytic properties, *IOP Conf. Ser.:Mater. Sci. Eng.*, 2016, **107**, 012006.
53 H. Kahler, The Crystalline Structures of Sputtered and Evaporated Metallic Films, *Phys. Rev.*, 1921, **18**, 210–217.
54 H. Yang, G. Yang, Z. Qiao, Y. Yang, S. Zhang, X. Li and Y. Liu, Ultrafast synthesis of surface defect-modified Bi/BiOCl nanosheets via the deflagration of NaN_3 for solar water evaporation, *J. Alloys Compd.*, 2020, **836**, 155380.
55 S. Yang, H. An, S. Arnouts, H. Wang, X. Yu, J. de Ruiter, S. Bals, T. Altantzis, B. M. Weckhuysen and W. van der Stam, Halide-guided active site exposure in bismuth electrocatalysts for selective CO_2 conversion into formic acid, *Nat. Catal.*, 2023, **6**, 796–806.
56 V. G. Gattow and D. Schütze, Über Wismutoxide. (VI) Überein Wismut(III)–oxid mit höherem Sauerstoffgehalt (β–Modifikation), *Z. Anorg. Allg. Chem.*, 1964, **328**, 44–68.
57 H. Kageyama, K. Hayashi, K. Maeda, J. P. Attfield, Z. Hiroi, J. M. Rondinelli and K. R. Poeppelmeier, Expanding frontiers in materials chemistry and physics with multiple anions, *Nat. Commun.*, 2018, **9**, 772.
58 S. D. Young, B. M. Ceballos, A. Banerjee, R. Mukundan, G. Pilania and B. R. Goldsmith, Metal Oxynitrides for the Electrocatalytic Reduction of Nitrogen to Ammonia, *J. Phys. Chem. C*, 2022, **126**, 12980–12993.

